# Design and calibration of field deployable ground-viewing radiometers

Nikolaus Anderson,[1,*] Jeffrey Czapla-Myers,[1] Nathan Leisso,[2] Stuart Biggar,[1] Charles Burkhart,[1] Rob Kingston,[1] and Kurtis Thome[3]

[1]Remote Sensing Group, College of Optical Sciences, University of Arizona, 1630 East University Boulevard, Tucson, Arizona 85721, USA

[2]Currently with National Ecological Observatory Network, 1685 38th Street, Suite 100, Boulder, Colorado 80301, USA

[3]NASA Goddard Space Flight Center, Greenbelt, Maryland 20771, USA

*Corresponding author: nanderson@optics.arizona.edu

Three improved ground-viewing radiometers were built to support the Radiometric Calibration Test Site (RadCaTS) developed by the Remote Sensing Group (RSG) at the University of Arizona. Improved over previous light-emitting diode based versions, these filter-based radiometers employ seven silicon detectors and one InGaAs detector covering a wavelength range of 400–1550 nm. They are temperature controlled and designed for greater stability and lower noise. The radiometer systems show signal-to-noise ratios of greater than 1000 for all eight channels at typical field calibration signal levels. Predeployment laboratory radiance calibrations using a 1 m spherical integrating source compare well with in situ field calibrations using the solar radiation based calibration method; all bands are within ±2.7% for the case tested.  © 2013 Optical Society of America

*OCIS codes:*    130.6010, 230.0040, 280.4788, 280.4991.

## 1. Introduction

The knowledge of the radiometric calibration of Earth observing satellites has been shown to be critical to the success of these sensor systems. Pre- and post-launch radiometric calibration are necessary to accurately define the calibration of a satellite sensor over time [1,2]. The Remote Sensing Group (RSG) at the University of Arizona has provided pre-flight and post-launch radiometric calibrations for many satellite and airborne systems since the mid-1980s [3,4]. A majority of this work at RSG has been with post-launch (or in-flight) calibration; specifically vicarious calibration using the reflectance-based method. The accuracy of the reflectance-based method has improved over time as equipment and procedures are upgraded, in many instances as low as 1.5%–2.5%

uncertainty [5]. The manned vicarious calibrations provided by RSG have been helpful to numerous satellite and airborne systems [6–8].

Typical RSG vicarious calibration, as detailed in [9], has some drawbacks. The cost and time required for personnel on-site for each calibration limits the number of vicarious calibrations attempted. Among other reasons, this is why the Radiometric Calibration Test Site (RadCaTS) was developed as an automated, unmanned calibration approach beginning in 2004 at a proven RSG vicarious calibration test site: Railroad Valley (RRV) dry lake bed, Nevada [10]. The RadCaTS concept mimics the basics of the reflectance-based vicarious calibration with three main sets of data needed at the time of satellite overpass: atmospheric transmission measurements, ancillary meteorological measurements, and surface reflectance measurements. Atmospheric measurements are made with an Aerosol Robotic Network (AERONET) Cimel sun photometer [11],

meteorological station data are recorded and surface reflectance measurements are made with ground-viewing radiometers (GVRs). Surface reflectance, or more specifically for this work bidirectional reflectance factor (BRF) [12] is determined for the surface of interest in each case. All of these are used as inputs into a customized, RadCaTS-specific radiative transfer code that utilizes current MODTRAN [13] software.

At its onset, the RadCaTS site was populated with radiometers using LEDs as the optical detector. The concept of producing low cost radiometers with a somewhat limited spectral responsivity has been employed in many scenarios [14–18]. Over the years of initial GVR deployment, more LED radiometers were built and installed to improve spatial sampling of the test site. Improvements were also made to the optical design of these radiometers, and by 2007 the site was outfitted with five three-channel LED radiometers that employed a two-lens collector containing an objective and field lens [19].

The results of this initial RadCaTS site were promising given the fact that the radiometers were built and deployed under requirements to use low cost parts yet still be capable of autonomous field operation. In comparison to the typical RSG vicarious calibration method, the results showed higher variability. Yet the sheer quantity of data and the production of results usable as a secondary means of monitoring sensor calibration showed that the automated site was a useful means of vicarious calibration.

Several studies were performed to assess the usability of these data and ways to improve the results from the automated site. Initially, the effort was focused on determining how many radiometers were necessary to achieve a spatial average of the test site [20]. This topic is specific to the resolution of the airborne or satellite sensor in question and the area being sampled. However, it was deemed that for this site at RRV, a reasonably small number of radiometers (four) would be able to produce an average reflectance indicative of the entire site. In this evaluation process, it became apparent that the quality of results, after installing a required number of radiometers, was directly tied to the quality of the reflectance data as measured by the GVRs [21]. Thus, a major focus of recent improvement to the RadCaTS site has been the design, construction, and deployment of improved GVRs.

## 2. Radiometer Concept

The LED-based radiometers used as GVRs during the initial population of the RadCaTS site were produced with a prior understanding of their limitations. Due to funding and other factors it was decided that a proof of concept site was necessary, and LED radiometers achieved this goal. However, the limiting factor in the accuracy of the RadCaTS results was the performance of the radiometers, so new and improved versions were developed.

A few particular shortcomings of the LED-based design continuously affected the results from the early RadCaTS site. Commercially available LEDs tested by RSG were limited in spectral variety and had moderately wide (50 nm or greater) spectral bandpasses, which were often asymmetric about center wavelength [19]. For these reasons, and initial data logger limitations, the LED-based radiometers included three detectors. This limited the knowledge of the spectral shape of the ground reflectance in the typical spectral range of interest (350–2500 nm) during field operation. Figure 1 shows a sample reflectance of RRV playa as measured by a field spectrometer during typical RSG reflectance retrieval detailed in [9]. The full width at half maximum (FWHM) bandwidth of each of the three LED channels is highlighted.

In addition, LEDs, when used as detectors, are particularly sensitive to temperature. Not only is there a change in dark current and thus measured signal (as with most photosensitive devices), there is also a change in spectral responsivity with temperature [15]. Also, the lack of sensitivity of LEDs required a powered optical solution to increase throughput for the LED radiometers. The design chosen for this was a two-lens system consisting of an objective and a field lens placed at the image plane of the objective. This concept was utilized in order to help provide a more even illumination to the LED detector plane [19,22]. This method was operational, however, once in the field it was noted that the front (objective) lens was often found quite dirty, even while being somewhat shrouded by its housing. This is a problem in terms of throughput for any optical system, and in the case of the LED-based GVRs, the problem was exacerbated by the fact that the field lens focuses an image of the objective lens onto the LED detector plane. Any obscuration at that surface is focused on the detectors, making a potentially minor
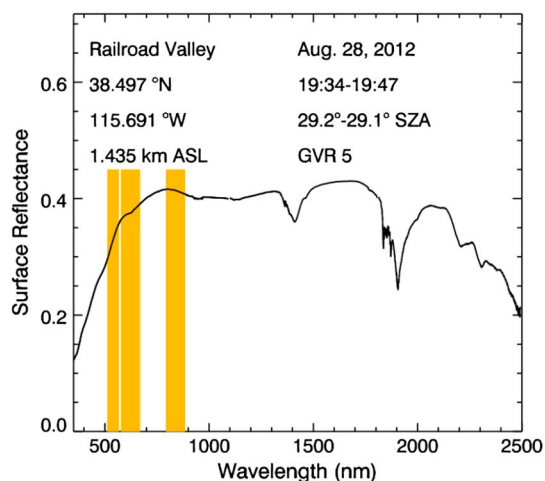


Fig. 1. (Color online) Typical spectral reflectance of RRV dry lake. FWHM bandwidth information for LED radiometer channels is depicted as the width of the (yellow) rectangles. The height of the rectangle is arbitrary. ASL, above sea level; SZA, solar zenith angle.

throughput problem a major location dependent (and therefore channel dependent) problem based entirely on where dirt or mud collects.

These important lessons learned with the LED radiometers, coupled with the group's experience making high quality laboratory transfer radiometers [23–26], provided a strong basis for a new radiometer design. Sparked by new funding and the aforementioned research that showed a necessity for higher quality reflectance measurements, RSG decided to construct a more traditional radiometer that uses interference filters coupled with well-understood stable detectors.

Optical detection is accomplished using seven silicon detectors and one InGaAs detector that are housed in individual modules. Figure 2 shows a module and associated layout. An interference filter with an approximate 20 nm bandpass (FWHM) is located in front of the rear aperture for spectral selection. The two apertures fully limit the field-of-view (FOV) of the module (or "channel"), although additional apertures at the front of the system are used as stray light baffles. Eight channels, seven VNIR and one SWIR, make up the detector plane of the new GVR.

The baseplate of each module has a 2° angle, which allows each channel to view the same section of ground. The eight modules are mounted in a circular pattern and the tilt directs the center of each channel FOV toward the vertical centerline of the instrument as viewing nadir. When the radiometer is mounted at 1.5 m, the center of the FOV projection for each channel matches on the ground. This allows for the system to be optically unpowered yet have little effect from spatial variation viewing different areas of the site. The decision to tilt at 2° was a balance between the height of the mount and an effort to minimize the view angle from nadir. Previous work has shown that the BRF of RRV is consistent for near-nadir view angles [27]. This supports the notion that tilting the focal plane in this manner should not be a cause for concern with respect to directional dependence of the surface reflectance.

Figure 3 shows the RRV playa surface with a sample GVR FOV projection. This FOV, nominally 10° full field, was implemented for similarity to the 11° nominal FOV of the previous LED version radiometers [19]. The size of the approximate projection on the ground depicted in the figure is calculated using the theoretical FOV of each instrument (19.3 cm for LED version and 26.2 cm for current
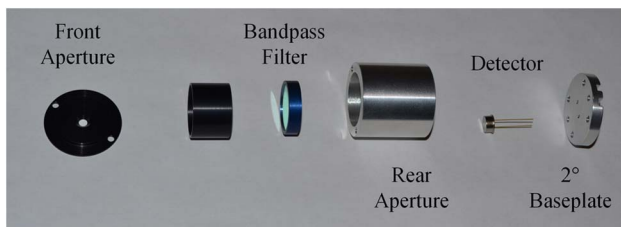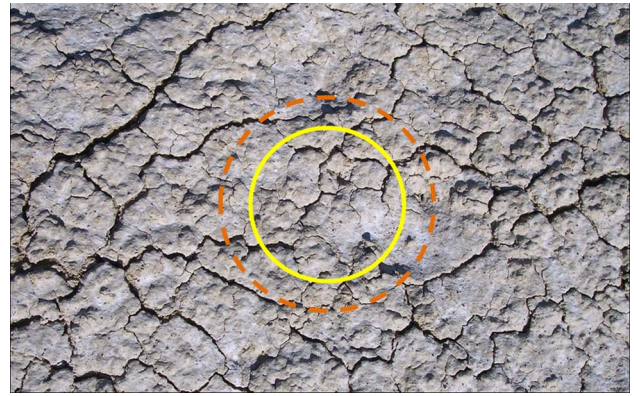


Fig. 3. (Color online) RRV dry lake surface with approximate ground projection of LED FOV (solid circle) and GVR FOV (dashed circle).

GVR). More information regarding FOV, including characterization, is included in section four. Due to the greater height of the mounted radiometer, the resulting area on the ground detected by the current GVR is 36% greater than previous radiometers, which should result in a slightly better spatial average of surface features.

For improved stability and accuracy of reflectance measurements, GVRs have been outfitted with a thermal stabilization system utilizing a thermoelectric (TE) cooler. While not as susceptible to thermal variations as the LED-based radiometers, there is still a need for thermal control to keep these band-dependent variations to a minimum. The thermal control, however, is quite costly with respect to power for this autonomous system so the thermal system only operates when there is ample signal as read by the 850 nm detector channel. This control was implemented to ensure the system does not waste power over night or during very cloudy periods. There is more information about the thermal control system in the following section.

## 3. System Design and Implementation

At the time of this publication three updated GVRs have been produced at RSG: GVR 21, 22, and 23. GVR 21 was deployed initially in May 2011. After GVR 21 was built and deployed, some design upgrades were implemented into the production of GVR 22 and 23, which were built simultaneously and deployed during October 2011. GVR 21, because of its production as prototype for the new GVR design, has some unique features. They will be mentioned where appropriate, but in a general sense the design discussed in this paper will be that of GVR 22 and 23. Figure 4 contains a photo of GVR 23 as deployed.

The GVR data scheme is relatively simple. The voltage output from all eight channels, system voltage, temperature of the detector array baseplate and other ancillary information is logged by a data logger every two minutes. Power to the logger and signal electronics is continuously provided and the two minute data interval is constant during typical



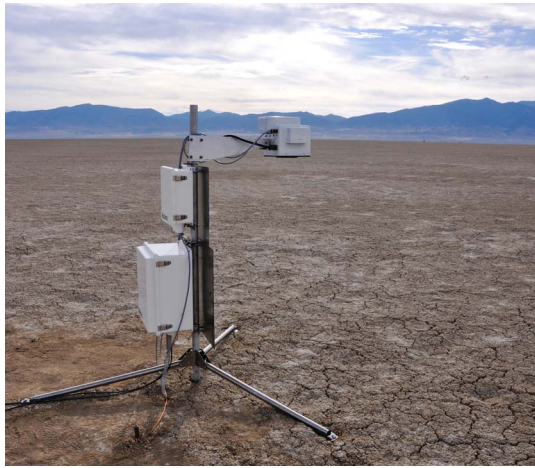Fig. 2. (Color online) Single GVR module assembly.

Fig. 4.   (Color online) GVR 23 deployed at RRV, Nevada.

operation. However, power to the thermal control system is only supplied based on logged events. Logic in the data logger toggles a solid state relay to power the thermal system. The thermal system is switched on when signal from the 850 nm detector channel crosses a set threshold voltage.

GVRs are outfitted with data loggers, which have 18 bit effective resolution for analog voltage measurements. After issues with LED radiometer data loggers collecting with 8 bit resolution, it was decided that much greater accuracy and resolution was needed to adequately make use of the performance improvements of new GVRs. The loggers are also designed to operate in temperatures found inside enclosures in field environments. The logger's logic and output customization available also makes it very convenient for dynamically controlling the power output for the TE cooling system via thresholds set on logged data.

### A.   Signal Electronics Design

The electronics associated with the GVR detector plane are shown in Fig. 5. A custom circuit board with seven layers was designed to house the necessary signal amplification electronics and associated noise reduction components. Although the circuit is based on a fairly standard signal amplification design using operational amplifiers, the complexity of the circuit is compounded by space, accuracy, and thermal requirements.

Because the system was designed to have temperature control for the detector area, it was decided to include the circuit board and signal electronics in the temperature controlled area. The most temperature-sensitive components are mounted on the underside of the circuit board closest to the temperature controlled aluminum base. The board is also surrounded by an insulator to help ensure the entire board is receiving at least some degree of temperature control. Temperature is not monitored at the board (it is monitored nearby on the baseplate), but the system results appear to show that the electronics are performing consistently.
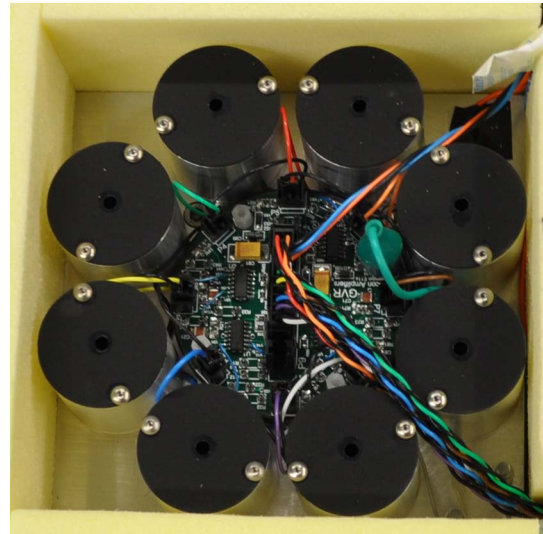


Fig. 5.   (Color online) Front view of GVR head. The eight modules surround the detector amplifier board and electronics.

More can be found on system performance in later sections.

### B.   Thermal Control

The head of the GVR is split into two sections. The internal view in Fig. 5 shows the front (or lower section as deployed), temperature controlled section of the head. This section houses all the detector channel assemblies along with the signal electronics and associated parts. Behind the temperature controlled aluminum base is the thermally uncontrolled side, which houses mainly the hot side of the TE cooler, including the heat sink and cooling fan. Both sections are exposed in the internal assembly photo Fig. 6.

The TE cooler system used is a 12 V, 36 W TE cold plate system, which means that the temperature control is delivered via direct contact as opposed to an air cooler. This allows better thermal control of the most important components; in this case the detectors and the detector channels. The system is
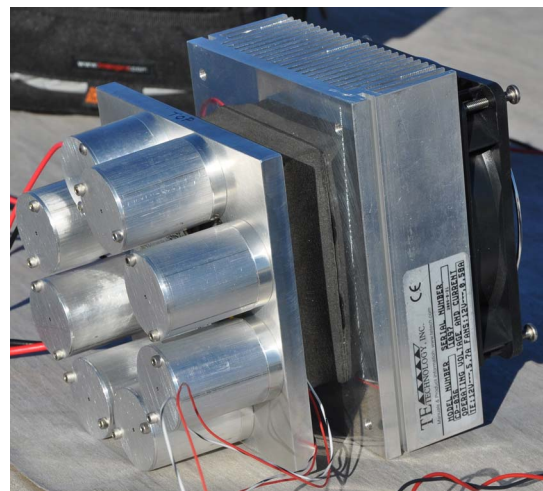


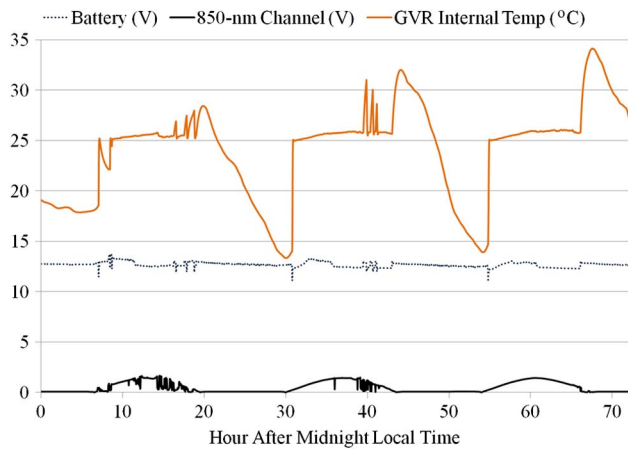Fig. 6.   (Color online) Internal GVR mechanical assembly.

Fig. 7. (Color online) Three days of GVR 22 operation during July 2012. Plot includes thermal and power data during clear and cloudy periods.

controlled via a bidirectional temperature controller set to 25°C. The thermal control is set using a 15 kΩ thermistor as the control temperature monitor, and a high quality thermistor mounted near a detector channel on the baseplate is logged as an independent temperature measurement.

Figure 7 shows examples of the day-to-day operation of a GVR with specific attention to the thermal and power characteristics encountered in different conditions. The "on" event can be noted in this plot where the logged system power voltage briefly drops, and "off" events typically appear in this plot as an increase in logged voltage. A good example of an "on" event for a day occurs near hour 31 where the short monitored voltage drop can be seen and the GVR temperature climbs quickly during initial TE system heating. The final "off" event for that day occurs near hour 42 where the logged voltage quickly increases a small amount and the GVR temperature rises to approximately 32°C before falling during the night. These events are the points during which power to the TE cooling system is turned on (if above threshold) or off. Currently, this is set by the 850 nm channel of the GVR and the value is chosen to ensure morning operation commences well prior to a typical overpass of interest (~10:30 local time or after) in the winter. The 850 nm channel was chosen due to its relatively low gain (due to high silicon responsivity and high signal), high and spectrally flat site reflectance, and low temperature dependence. The goal is to set the point such that summer thermal operation doesn't last longer than is necessary, and very cloudy periods also turn off the TE operation. This set point could be further researched to the point of providing more overall power efficiency, but thus far the system operation has supported set points that are likely safer than necessary to ensure no required data are missed.

## C. System Power Architecture

In order to accomplish all the goals of improved performance for the new GVRs, it is necessary to have a
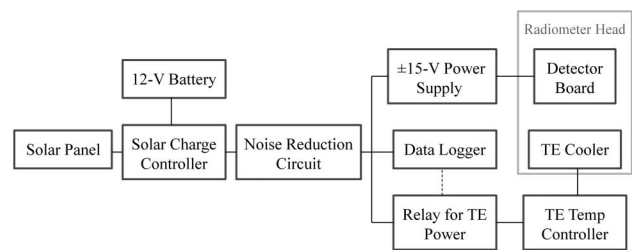


Fig. 8. GVR system power block diagram.

fairly complex, high-wattage power scheme. Specifically, the requirement for thermal control drives the need for high power consumption at times. A solar-charged high-amperage battery system is used for this purpose and is also used for the entire system power. However, power needs for the various elements in this system require a customized solution. A block diagram outlining the power scheme for the GVR is shown in Fig. 8.

The system power architecture for the GVR went through several iterations during testing, including an implementation quite different from Fig. 8 in GVR 21. The lessons learned led to this system design and it has performed quite well to date. Only fairly minimal, easily explained and corrected power losses have occurred in GVR 22 and GVR 23. At the time of this article this means that the GVRs have performed well during the lowest solar charging period (winter) and the highest power consumption period (summer).

The sizing of the solar panel and battery was chosen to accommodate system power parameters. The 40 Ah battery should power the system without charging in 40% of max TE power cooling conditions (very high thermal conditions and atypical during witnessed field conditions) for 2 days of operation (a maximum of 12 h a day). Without thermal control operating (i.e., very cloudy conditions) the large battery would power the remainder of the system for several weeks. The 190 W solar panel should be capable of recharging a near depleted battery during system operation in one day during fair solar conditions. The solar charging, battery and general load circuit is controlled by a maximum power point tracking (MPPT) solar charger capable of a maximum of 15 A output to load and/or battery.

The MPPT charge controller, and likely any switching controller, provided some problems on the load line supplying the sensor and system. High frequency noise on the load line was measured at approximately 3 V peak-to-peak (p-p) during operation. This was discovered when components suffered serious operation degradation. In the case of the TE controller, it was unable to toggle power to the cooler thus rendering the thermal control useless. To combat these issues, a simple but robust noise reduction circuit was built onto the load output from the MPPT. Two matched high power and high value electrolytic capacitors are wired in parallel with a large toroidal inductor bridging their connection. Another lower

value high quality Teflon capacitor is also wired parallel to help reduce the higher frequency noise. The result is a load output with measured noise less than 40 mV p-p during operation and is adequate for noise control during operation of the entire system.

This power output, after the noise filtering, is sent to three parallel operations (again seen in Fig. 8). The data logger is powered continuously from this output. The thermal control is also powered from this output but its power is controlled via the data logger as mentioned in previous sections. The signal electronics, on the other hand, need positive and negative matched input voltages as is common for circuits utilizing operational amplifiers. In this case the dual output is supplied from a high quality switching power supply, which is powered by the main power output. This dual output supply is also wired with additional noise reduction components to ensure low noise on the power lines to the signal electronics.

## 4. System Characterization

Prior to field deployment, the GVRs were characterized and calibrated in the laboratories at RSG facilities. This section will include discussion of the instrument and component characterization; specifically the FOV measurements, signal-to-noise ratio (SNR) measurements, linearity measurements, filter transmittance measurements, and the selection of the radiometer's spectral bands.

A customized double monochromator is used for RSG filter (and other transmissive optics) transmission measurements. All filters were purchased commercially off the shelf and have a nominal bandwidth of 20 nm as specified by the manufacturer. The results from RSG filter transmission measurements confirmed the manufacturer bandwidths and out-of-band blocking. The results of the filter measurements performed are used as inputs into a GVR-specific radiative transfer code.

The decisions leading to filter center wavelength selections, while somewhat limited by commercial availability, were based on the spectral variability of the reflectance of the surface of interest: RRV dry lake bed. The spectral variability of the dry lake surface is largely dependent on moisture from rain and melted snow. Figure 9 shows a ratio of wet with respect to dry reflectance of the RRV site along with the selected GVR center wavelengths. The ratio was obtained from field spectrometer measurements the day prior to and the day after rain on the RRV site. The plot shows that knowledge of reflectance from 400 to 550 nm is important because of the spectral dependence of the reflectance change in this region. Also, the 1550 nm band will be able to help better predict the spectral reflectance in the SWIR region, which is also affected by water absorption. The effects and benefits of the spectral decisions and resulting data are one of the main topics of much current and future work. This work presented is limited to the GVR design and laboratory work, so discussion will be limited to the bearing that the
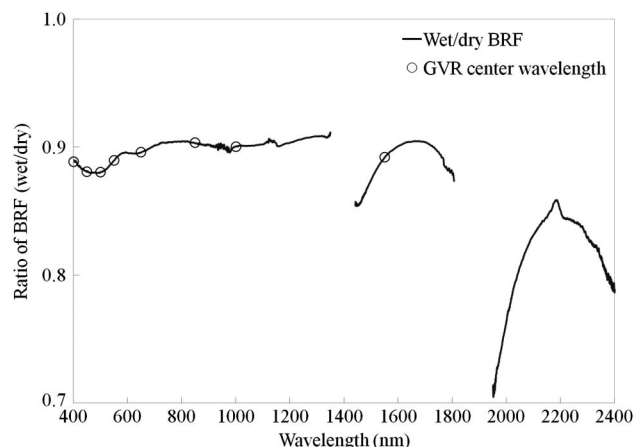


Fig. 9. Ratio of wet and dry RRV dry lake surface reflectance with noted GVR center wavelengths.

RRV playa spectral reflectance has on the design decisions.

Laboratory FOV measurements were performed using a 15 cm off-axis collimator with a small spherical integrating source (SIS) illuminating the collimator's input pinhole. The radiometer was placed on a rotary stage with the plane of the eight entrance apertures mounted at the center of rotation of the stage. Results from this testing are shown in Figs. 10 and 11. The data presented in Fig. 10 are normalized to maximum response, and horizontally shifted to center the maximum at 0° (normal) relative to the source. The figure depicts the full range of angles measured and data are presented in logarithmic scale to study potential stray light issues, which appear minimal. As is expected, the unshifted data shows that the center of the FOV varies horizontally depending on the physical location of the channel relative to the placement of the radiometer. Thus the 2° tilt of the focal plane is seen as a variation of the center of the FOV. An example of this is shown in Fig. 11 and confirms that the physical 2° tilt for each spectral channel measures optically as expected.

Linearity, SNR, and calibration measurements were made using a 1 m diameter SIS with a 35 cm
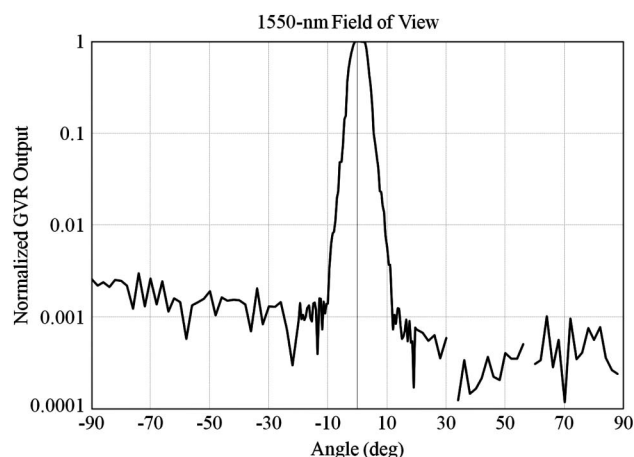


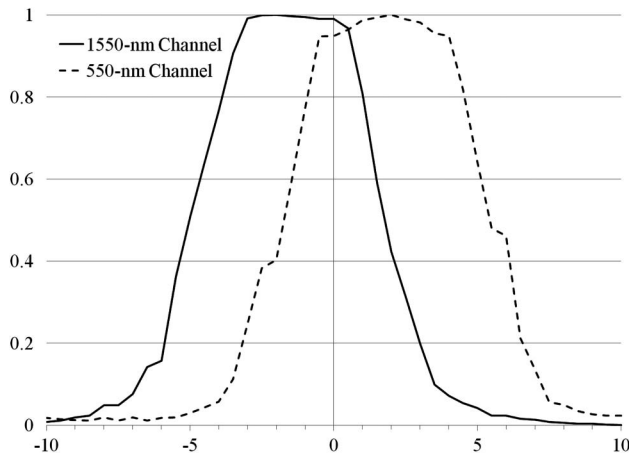Fig. 10. GVR 22 channel 8 laboratory FOV measurements.

Fig. 11. GVR 22 FOV measurements showing results of two opposing tilted channels.

diameter port. Calibration of the GVRs is discussed in detail in the following section. SNR measurements were extracted from the calibration measurements, and linearity characterization was accomplished by turning off lamp sources in the SIS. A total of 10 bulbs are used at the highest radiance level, and the number of operating bulbs is decreased over time as some GVR spectral channels saturate at higher SIS output levels. Linearity measurements showed that the GVRs are linear to the level that could be tested with this source apparatus and reference radiometer. The reference radiometer in this case, an Analytical Spectral Devices Inc. field spectrometer, has been reported in other lab tests to be linear on the 0.1% level [28]. Table 1 summarizes the results of the SNR tests. GVR 21 results are not included as some of the calculated SNR values are artificially high due to utilization of a different (12 bit resolution) data logger in that system.

## 5. System Calibration

RSG produced radiometers requiring radiance calibration, especially those used in the field, are often calibrated using both laboratory and outdoor methods [23,29]. Recently in the lab, the radiometers are typically calibrated either by viewing at 45° incidence a NIST calibrated Spectralon panel illuminated by a NIST irradiance lamp standard, or by directly viewing a 1 m SIS. The NIST standard method [30] is preferred for the most accurate calibrations, however, in the case of an instrument with a large FOV this method can be difficult to accurately accomplish. In the case of the GVR, the NIST standard method was abandoned. The relatively large

FOV of the GVR creates a problem: the NIST lamp standard, which is placed 50 cm away from the panel, illuminates the panel in the center with a given irradiance. Cosine falloff results in incident irradiance reduction further away from the center of the panel. More specifically, at approximately 4 cm away from the panel center the incident irradiance has fallen by 1%. To minimize this effect, some instruments with larger FOVs are placed as close as possible to the panel without obstructing the light source. However, in the case of the GVRs the eight spectral channels only view the same region when they are 1.5 m away from the object to be viewed. At this distance the FOV on a panel is a restrictively large 26.2 cm diameter. For these reasons, laboratory calibrations of the GVRs were made using the 1 m SIS. In this method the output of the SIS is viewed simultaneously by RSG calibrated radiometers, which are used to transfer the calibration to the instrument of interest, in this case the GVR.

With past ground radiometer instrumentation, SRBC was used almost exclusively for system calibration due to temporal changes in the LED-based radiometers. SRBCs can be performed on GVRs in the field and are thus much more logistically reasonable for field-deployed radiometers that require frequent calibration. However, SRBCs can be somewhat time intensive during field work, and more importantly require stable atmospheric conditions and multiple calibrations to maximize the accuracy of this calibration method.

The SRBC method has been discussed in depth in various publications [19,23,29,31,32]. To summarize, for this case of GVR SRBC, three types of GVR measurements are made within a short period of time: dark measurements, measurements of a white diffuser illuminated by all ambient light (including solar), and measurements of a white diffuser with the direct solar illumination physically blocked by an occulting disk. The white diffuser used is a 46 cm square Spectralon panel that is leveled and centered below the radiometer. It is fully characterized in the RSG laboratory for spectral BRF as detailed in [33].

Figures 12 and 13 depict the two calibration methods. As previously mentioned, the laboratory radiance calibration in this case is provided by a SIS being simultaneously monitored by a calibrated RSG radiometer. (In this case an Analytical Spectral Devices Inc. field spectrometer was used.) The SIS provides the radiance that is monitored by both instruments. The radiance calibration coefficient for a given radiometer channel, $k_i$, is calculated from the band-averaged hyperspectral radiance as

Table 1. Laboratory SNR Results for GVRs 22 and 23 at Typical SRBC Signal Levels

|        | 400 nm | 450 nm | 500 nm | 550 nm | 650 nm | 850 nm | 1000 nm | 1550 nm |
|--------|--------|--------|--------|--------|--------|--------|---------|---------|
| GVR 22 | 1573[a] | 1731 | 3262 | 1750 | 1819 | 1641 | 1937 | 2371 |
| GVR 23 | 1725[a] | 4170 | 7043 | 7105 | 3206 | 3247 | 3743 | 4682 |

[a]400 nm results are estimated using laboratory data scaled to typical solar radiation based calibration (SRBC) signal levels. This was done because signal in this spectrum from the SIS is too low to estimate levels seen in the field.

Fig. 12. (Color online) SRBC of GVR 21 at RRV, Nevada (Nathan Leisso pictured). Nathan is holding the occulting disk used to shade the Spectralon panel during diffuse measurements.

measured by the spectrometer, $L_{e\lambda}$ (which is dark corrected in the instrumentation software, and has units of $W \cdot m^{-2} \cdot sr^{-1} \cdot \mu m^{-1}$), and the dark corrected voltage output for the GVR channel, $V_i$, as in (1).

$$k_i = \frac{L_{e\lambda}}{V_i}. \qquad (1)$$

In the case of an SRBC, the calculations are more involved. In order to ensure GVR output used for the calibration is due only to radiance from the calibrated white Spectralon panel with illumination provided by the attenuated direct solar beam, the dark



Fig. 13. (Color online) GVR and ASD spectrometer (in the foreground on tripod mount with fiber optic exiting to the rear) viewing the SIS during laboratory calibration.

corrected average voltages from the GVR while shaded by an occulting disk, $V_{diffuse}$, is subtracted from the unshaded GVR output, $V_{global}$, as in (2).

$$V_{direct} = V_{global} - V_{diffuse}. \qquad (2)$$

Similar to Eqs. (1), (3) shows the calculation of the SRBC calibration coefficient.

$$k_i = \frac{L_{e\lambda}}{V_{direct}}. \qquad (3)$$

However, the radiance term in Eq. (3) is much more involved. The radiance is a product of the attenuated direct solar beam incident on the diffuser. Equation (4) shows this relationship [29].

$$L_{e\lambda} = \frac{\rho}{\pi} E_{o\lambda} e^{-m\delta_\lambda} \tau_{gas} \cos \theta. \qquad (4)$$

The other terms in Eq. (4) are as follows:

$\rho$ is the band-averaged reflectance factor of the panel diffuser.
$E_{o\lambda}$ is the spectral solar irradiance at the top of the atmosphere (TOA) corrected for earth-sun distance (typical units of $W \cdot m^{-2} \cdot \mu m^{-1}$).
$\delta_\lambda$ is the total optical depth for a vertical path through the atmosphere at the wavelength of interest as derived from coincident measurements by an RSG manufactured automated solar radiometer [34].
$m$ is the airmass that converts vertical optical depth to a slant path as based on [35].
$\tau_{gas}$ is the band-averaged gaseous transmittance.
$\theta$ is the solar zenith angle (SZA) in this SRBC case.

The expected SRBC uncertainty is approximately 3% [23]. A lab radiance calibration using a NIST standard has an approximately 2% uncertainty [23]. In this GVR case the calibration is not a direct NIST standard calibration and there is added uncertainty due to the spectrometer repeatability characteristics. Yet based on results with these spectrometers such as those reported in [28], the added uncertainty should not result in greatly increased uncertainties when the spectrometers are properly used, thus the previous claim of an uncertainty for laboratory calibration of approximately 2% should be valid for this use.

Table 2 summarizes the calibration results for GVR 23. Laboratory calibrations have been performed on all three radiometers and SRBCs have been performed on GVRs 21 and 23 at the time of this publication. GVR 21 results are omitted due to changes made to the system during this time period. The GVR 23 results presented here were performed as detailed in the previous paragraphs and calculated using the equations and equipment defined. The SRBC results presented are from a calibration collected at RRV playa during November 2011. The GVR 23 results represent expected results from GVR calibration barring radiometer changes over

**Table 2.  Laboratory and Field Calibration Results for GVR 23[a]**

|  | 400 nm | 450 nm | 500 nm | 550 nm | 650 nm | 850 nm | 1000 nm | 1550 nm |
|---|---|---|---|---|---|---|---|---|
| Lab Cal | 217.1 | 144.5 | 161.3 | 143.6 | 153.0 | 87.5 | 68.2 | 14.5 |
| SRBC | 211.2 | 144.0 | 159.1 | 144.1 | 155.5 | 88.0 | 69.7 | 14.5 |
| Difference | −2.7% | −0.4% | −1.4% | 0.3% | 1.7% | 0.5% | 2.2% | −0.2% |

[a]SRBC results presented here are calculated using TOA irradiance from [36]. The calibration coefficients, $k_i$ as previously defined, have units of $[(\mathrm{W} \cdot \mathrm{m}^{-2} \cdot \mathrm{sr}^{-1} \cdot \mu\mathrm{m}^{-1})\mathrm{V}^{-1}]$.

time. They show differences less than the uncertainties for the two calibration methods and move toward proving that SRBCs can be treated as calibration checks for these instruments rather than relying on the SRBC to account for major temporal variations, which is the case for previous radiometers. However, SRBCs are likely necessary to evaluate changes as the radiometer calibration, and especially field related calibration issues (dirty windows or similar) are likely to change over time. Ideally, radiometers would be calibrated in the laboratory as often as once a year to ensure accurate, current calibration results. However, this is difficult with the current suite of instruments because of the lack of redundant radiometer equipment.

## 6. Conclusions

Three improved GVRs have been produced and are currently deployed at RRV dry lake bed, Nevada, in support of RSG automated vicarious calibration work. Radiometric calibrations and laboratory characterizations have been performed and imply that the radiometers are working properly and represent a significant improvement over previous LED-based radiometers.

Current and future work, including initial work in [37], will address the improvements in the overall quality of the vicarious calibration results provided from the automated test site. The goal of radiometer improvements is to achieve RadCaTS uncertainty on the level of typical RSG in situ measurements. Temporal variations of the new radiometers, especially due to field conditions, must be further studied to assess their help in achieving this goal. Also, increased production of improved GVRs is necessary to fully phase out the LED radiometers. Ideally five or more new GVRs would be operational, with one full spare always housed at RSG laboratories. This would allow long-term controlled experiments, better and faster troubleshooting and fixing of GVR issues, and provide an easy way to accomplish more laboratory calibrations without interrupting data collection.

## References

1. J. J. Butler and R. A. Barnes, "Calibration strategy for the Earth Observing System (EOS)-AM1 platform," IEEE Trans. Geosci. Remote Sens. **36**, 1056–1061 (1998).
2. N. Fox, A. Kaiser-Weiss, W. Schmutz, K. Thome, D. Young, B. Wielicki, R. Winkler, and E. Woolliams, "Accurate radiometry from space: an essential tool for climate studies," Philos. Trans. R. Soc. **369**, 4028–4063 (2011).
3. P. N. Slater, S. F. Biggar, R. G. Holm, R. D. Jackson, Y. Mao, M. S. Moran, J. M. Palmer, and B. Yuan, "Reflectance-and radiance-based methods for the in-flight absolute calibration of multispectral sensors," Remote Sens. Environ. **22**, 11–37 (1987).
4. P. N. Slater, S. F. Biggar, J. M. Palmer, and K. J. Thome, "Unified approach to absolute radiometric calibration in the solar-reflective range," Remote Sens. Environ. **77**, 293–303 (2001).
5. D. Helder, K. Thome, D. Aaron, L. Leigh, J. Czapla-Myers, N. Leisso, S. Biggar, and N. Anderson, "Recent surface reflectance measurement campaigns with emphasis on best practices, SI traceability and uncertainty estimation," Metrologia **49**, S21–S28 (2012).
6. K. J. Thome, S. F. Biggar, N. Anderson, J. Czapla-Myers, R. B. Lockwood, S. J. Miller, T. W. Cooley, T. G. Chrien, S. J. Schiller, J. F. Silny, and M. A. Glennon, "Preflight and vicarious calibration of Artemis," in *Geoscience and Remote Sensing Symposium (IGARSS 2008)* (IEEE, 2008), Vol. **1**, pp. I-249–I-252.
7. K. J. Thome, K. Arai, S. Tsuchida, and S. F. Biggar, "Vicarious calibration of ASTER via the reflectance-based approach," IEEE Trans. Geosci. Remote Sens. **46**, 3285–3295 (2008).
8. B. L. Markham, M. O. Haque, J. A. Barsi, E. Micijevic, D. L. Helder, K. J. Thome, D. Aaron, and J. S. Czapla-Myers, "Landsat-7 ETM+: 12 years on-orbit reflective-band radiometric performance," IEEE Trans. Geosci. Remote Sens. **50**, 2056–2062 (2012).
9. K. J. Thome, "Absolute radiometric calibration of Landsat 7 ETM+ using the reflectance-based method," Remote Sens. Environ. **78**, 27–38 (2001).
10. K. P. Scott, K. J. Thome, and M. R. Brownlee, "Evaluation of the Railroad Valley Playa for use in vicarious calibration," Proc. SPIE **2818**, 158–166 (1996).
11. B. N. Holben, T. F. Eck, I. Slutsker, D. Tanré, J. P. Buis, A. Setzer, E. Vermote, J. A. Reagan, Y. J. Kaufman, T. Nakajima, F. Lavenu, I. Janjowiak, and A. Smirnov, "AERONET—a federated instrument network and data archive for aerosol characterization," Remote Sens. Environ. **66**, 1–16 (1998).
12. G. Schaepman-Strub, M. E. Schaepman, T. H. Painter, S. Dangel, and J. V. Martonchik, "Reflectance quantities in optical remote sensing—definitions and case studies," Remote Sens. Environ. **103**, 27–42 (2006).
13. A. Berk, P. Acharya, G. Anderson, and B. Gossage, "Recent developments in the MODTRAN atmospheric model and implications for hyperspectral compensation," in *Geoscience and Remote Sensing Symposium (IGARSS 2009)* (IEEE, 2009), Vol. **2**, pp. II-262–II-265.

14. F. M. Mims III, "Sun photometer with light-emitting diodes as spectrally selective detectors," Appl. Opt. **31**, 6965–6967 (1992).
15. Y. B. Acharya, A. Jayaraman, S. Ramachandran, and B. H. Subbaraya, "Compact light-emitting-diode sun photometer for atmospheric optical depth measurements," Appl. Opt. **34**, 1209–1214 (1995).
16. D. R. Brooks and F. M. Mims III, "Development of an inexpensive handheld LED-based Sun photometer for the GLOBE program," J. Geophys. Res. **106**, 4733–4740 (2001).
17. F. M. Mims III, "An inexpensive and stable LED Sun photometer for measuring the water vapor column over South Texas from 1990 to 2001," Geophys. Res. Lett. **29**, 20.1–20.4 (2002).
18. E. Miyazaki, S. Itami, and T. Araki, "Using a light-emitting diode as a high-speed, wavelength selective photodetector," Rev. Sci. Instrum. **69**, 3751–3754 (1998).
19. J. S. Czapla-Myers, K. J. Thome, and S. F. Biggar, "Design, calibration, and characterization of a field radiometer using light-emitting diodes as detectors," Appl. Opt. **47**, 6753–6762 (2008).
20. J. S. Czapla-Myers, K. J. Thome, B. R. Cocilovo, J. T. McCorkel, and J. H. Buchanan, "Temporal, spectral, and spatial study of the automated vicarious calibration test site at Railroad Valley, Nevada," Proc. SPIE **7081**, 70810I (2008).
21. J. S. Czapla-Myers, K. J. Thome, and N. P. Leisso, "Radiometric calibration of earth-observing sensors using an automated test site at Railroad Valley, Nevada," Can. J. Remote Sens. **36**, 474–487 (2010).
22. W. J. Smith, *Modern Optical Engineering*, 3rd ed. (McGraw-Hill, 2000).
23. S. F. Biggar, "Calibration of a visible and near-infrared portable transfer radiometer," Metrologia **35**, 701–706 (1998).
24. P. R. Spyak, D. S. Smith, J. Thiry, and C. J. Burkhart, "Shortwave infrared transfer radiometer for the calibration of the Moderate-Resolution Imaging Spectrometer and the Advanced Spaceborne Thermal Emission and Reflection Radiometer," App. Opt. **39**, 5694–5706 (2000).
25. S. F. Biggar, K. J. Thome, R. B. Lockwood, and S. Miller, "VNIR transfer radiometer for validation of calibration sources for hyperspectral sensors," Proc. SPIE **6677**, 66770W (2007).
26. N. J. Anderson, K. J. Thome, S. F. Biggar, and J. S. Czapla-Myers, "Design and validation of a transfer radiometer," Proc. SPIE **7081**, 708104 (2008).
27. K. J. Thome, N. Smith, and K. Scott, "Vicarious calibration of MODIS using Railroad Valley Playa," in *Geoscience and Remote Sensing Symposium (IGARSS 2001)* (IEEE, 2001), Vol. **3**, pp. 1209–1211.
28. J. J. Butler, S. J. Janz, B. C. Johnson, R. D. Saunders, J. W. Cooper, M. G. Kowalewski, and R. A. Barnes, "Calibration of a radiance standard for the NPP/OMPS instrument," Proc. SPIE **7106**, 71060Z (2008).
29. N. J. Anderson, S. F. Biggar, K. J. Thome, and N. P. Leisso, "Solar radiation-based calibration of laboratory grade radiometers," Proc. SPIE **6677**, 66770X (2007).
30. J. H. Walker, R. D. Saunders, J. K. Jackson, and D. A. McSparron, "NBS measurement services: spectral irradiance calibrations," (National Institute of Standards and Technology, 1987).
31. S. F. Biggar, P. N. Slater, K. J. Thome, A. H. Holmes, and R. A. Barnes, "Preflight solar-based calibration of SeaWiFS," Proc. SPIE **1939**, 233–242 (1993).
32. S. F. Biggar, K. J. Thome, P. R. Spyak, and E. F. Zalewski, "Solar-radiation based calibration in the range 740 to 2400 nm," Proc. SPIE **3870**, 228–233 (1999).
33. S. F. Biggar, J. Labed, R. P. Santer, P. N. Slater, R. D. Jackson, and M. S. Moran, "Laboratory calibration of field reflectance panels," Proc. SPIE **924**, 232–240 (1988).
34. A. R. Ehsani, J. A. Reagan, and W. H. Erxleben, "Design and performance analysis of an automated 10-channel solar radiometer instrument," J. Atmos. Ocean. Technol. **15**, 697–707 (1998).
35. F. Kasten and A. T. Young, "Revised optical air mass tables and approximation formula," Appl. Opt. **28**, 4735–4738 (1989).
36. World Climate Research Program (WCRP) Publication Series No. 7, WMO ITD—No. 149: 119–126 (1986). The data were compiled by C. Wehrli, World Radiation Center (NRC), Davos-Dorf, Switzerland, under WRC publication, No. 615 (1985).
37. J. S. Czapla-Myers, N. P. Leisso, N. J. Anderson, and S. F. Biggar, "On-orbit radiometric calibration of Earth-observing sensors using the Radiometric Calibration Test Site (RadCaTS)," Proc. SPIE **8390**, 83902B (2012).